Consequences of scattering for spectral imaging of turbid biologic tissue

Mark Arnoldussen[†], David Cohen*[†], Gregory Bearman[‡], Warren Grundfest[†]

[†]Laser Research and Technology Development Laboratory, Cedars-Sinai Medical Center, 650 S. San Vicente Blvd., Los Angeles, CA 90048

[‡]Jet Propulsion Laboratory, California Institute of Technology, Pasadena, CA 91109

ABSTRACT

Spectral imaging permits two-dimensional mapping of the backscattering properties of biological systems. Such mapping requires broadband illumination of the entire area of interest. However, imaging of turbid biological media under these conditions often involves mean photon path lengths that exceed the pixel size. Using a numerical Monte Carlo model, we have studied the effects of photon scattering in a hemoglobin-bearing model system. We find that photon migration and the resulting wavelength-dependent optical coupling between pixels can complicate the analysis of imaging spectroscopy data. In fact, the wavelength dependence of photon trajectories also alters the distribution of photon exit angles at the tissue surface. We therefore find that the finite optical field of view of an imaging spectrometer can affect the measured spectra in the absence of chromatic aberrations.

Keywords: hyperspectral imaging; reflection spectroscopy; monte carlo model; retina

corresponding author:
David Cohen
650 S. San Vicente Blvd., Los Angeles, CA 90048. tel: 310 855 2956
fax: 323 653 9415 email: cohendx@cshs.org

note: Preliminary results from this study were presented on January 25 at the 1999 SPIE annual meeting as part of the conference on Three-Dimensional and Multidimensional Microscopy (conference number 3605B).

1. Introduction

Until recently, optical backscattering and reflectance measurements of tissue in the biomedical literature have been made using fiber-optic probes or limited imaging systems. The addition of true imaging to biomedical spectroscopy can provide much more information than point spectroscopy alone. With enabling technologies that include active devices such as acousto-optical tunable filters, liquid crystal tunable filters, interferometry, as well as passive techniques such as diffractivè optics, one arrives at imaging spectroscopy. The end product of a true imaging spectrometer is the "image cube," which adds a third dimension of wavelength to the two spatial dimensions of the image. With this (x, y, λ) dataset, the user can classify and analyze pixels by their spatial and spectral tomography. The combination of morphology and spectral tagging provides the potential to evaluate composition information for non-invasive monitoring. New technologies in the past decade have prompted an array of applications of spectroscopy to biological and medical problems, including tumor and dysplasia detection by fluorescence, as well as fluorescent in-situ hybridization (FISH), related cytogenetic techniques, and histopathology[1,2].

The development of imaging spectroscopy has, until recently, been driven by the planetary remote sensing programs of organizations such as NASA[3]. Optical remote sensing of planetary surfaces reveals variations in surface composition by the corresponding variation in spectra of backscattered light. It is important to note that sensors on an orbiting platform are constrained to imaging geometries that differ greatly from those that obtain in biological imaging. When measuring spectra from a high altitude, the trajectory of a single photon is unlikely to encounter more than a single

species because the mean scattering length is orders of magnitude smaller than the length scales characteristic of composition change. Multiple species within a given pixel are predominantly sampled by separate photon trajectories, resulting in more linear (additive) mixing of spectra from each species, after all photons exiting the surface from a pixel are collected (in this paper, the term pixel is used to refer interchangeably to the individual sensing elements of a planar image sensor as well as to the corresponding elements of area on the object being imaged). It is then possible to estimate surface composition on each pixel using either *a priori* spectral reflectance data from the pure components, or even *ad hoc* methods based on significant statistical variations in measured spectral reflectance data.

In the ideal case, imaging spectroscopy offers the hope of obtaining similar information. However, the different length scales involved in biomedical optics require consideration: optical scattering within biological media leads inevitably to optical trajectories through multiple species. The backscattering spectra resulting from intimately commingled reflecting species must be interpreted carefully because spectra of individual components are not additive. Additionally, the strong scattering prevalent in biological media implies that photons scattered into any one field of view and subsequently imaged onto a pixel will have a broad distribution of path lengths, further complicating interpretation. The spectrum measured from a pixel may contain information sampled from the tissue of the surrounding volume because the effective size of the pixels imaged from the tissue surface are comparable or smaller than the mean path traveled by a diffuse photon. Because the shape of the average path is also a function of optical properties, the angular limitations of light collection may also affect the spectral results.

The distribution of the deflection angles is determined by the Henyey-Greenstein phase function with anisotropy parameter g. With this choice of phase function, the azimuthal scattering angle is uniformly distributed between 0 and 2π. To account for absorptive events, a fraction of the photon's weight is subtracted from the packet based on the length it has traveled in accord with Beer's law. Only the top and bottom of the tissue are permitted to reflect photon packets. When a diffuse photon reaches the surface, the probability of internal reflection based on Fresnel reflectance is computed. In the case of no reflection, the photon exits with angular trajectory based on Snell's law. When we consider using a model with a wavelength-dependent backing reflector, we treat it as a purely specular reflector.

We account for wavelength effects by iterating the code over multiple wavelengths with the wavelength variation of optical properties included. In order to assess trajectory effects on each packet, its necessary attributes are retained throughout the simulation, including the surviving weight associated with the packet, the coordinates of exit at the surface, the exiting angles, and the total optical path length traveled through each layer of the model. Photon path lengths are available *post priori* within any one layer or all layers combined. The photon exiting trajectories at the tissue surface will be used to determine which backscattered photons that successfully traverse an imaging system.

Other workers in the field have also numerically studied photon scattering using photon diffusion and related techniques[8]. Experimentally, the question has been approached using, for example, time-resolved photon scattering. The distribution of photon arrival times measured in these experiments also provides path length information

There is a growing body of retinal spectroscopy, for example, where this problem may become an issue[4,5,6].

This paper examines the relation between optical scattering and some realistic constraints in the case of a spectral imaging system and a backscattering target. We restrict our investigation to a single species in order to concentrate on effects arising from photon trajectory distributions. Specifically, we investigate effects of finite illumination geometry as well as finite field of view. To estimate the magnitude of these effects, we simulate an imaging system using a hybrid method, combining a Monte Carlo photon transport code inside the target with simple raytracing to implement imaging. Our model systems use oxyhemoglobin as a chromophore.

2. Methods

A. Monte Carlo Simulation

The basic structure of the model is similar to that put forth by Wang and Jacques[7]. We review the highlights of the method here for completeness. An infinitely narrow source of streaming photon packets is directed perpendicularly into the topmost layer of tissue. As each packet is launched into the tissue, the specular reflectance is subtracted. Once inside the tissue, the distance traveled by the packet is determined by sampling the probability distribution of the mean free path, which is a function of the absorption μ_a and scattering μ_s extinction coefficients. When the scattering behavior of the tissue is approximately known, the anisotropy factor g, which represents the average cosine of the deflection angle, is used to determine the direction of flight of the photon after collision.

because the transit time of each photon is related to its path length by the velocity of light in tissue[9].

B. Imaging

Rather than dwell on detailed raytracing calculations for a particular optical system, we assume an idealized 1:1 imaging system with selectable angular field of view. We implement imaging of backscattered light trivially as a mapping between the detector plane pixels and their projection on the tissue surface. Finite fields of view are implemented by rejection of those free space trajectories that fail to pass through the entrance pupil. Aberrations are beyond the scope of this initial study. We treat the limiting case of maximal angular field of view by assuming that all exiting photons can be analyzed by assuming a detector array coplanar with the tissue surface. In all cases discussed in this paper, the image plane is divided into square pixels 50 microns on a side.

C. Source Profile

We consider only homogeneous semi-infinite layers in this paper. Therefore, the symmetry of the phase function in this model simplifies simulation of the effects of a finite illumination area. A single simulation run generates a set of photon packets exiting our tissue surface in a region surrounding the entry point. More specifically, the run contains an approximate representation of the photon population $I(\vec{r})$ exiting the tissue at a displacement $\vec{r}$ from the source. We generate the effect of a finite illumination spot by

integrating the exiting photon populations resulting from sources at discrete points above the tissue within a circle of the desired diameter. We accomplish this by numerically by calculating the sum $\sum_{\{P\}} I_P(-\vec{r})$, where {P} is the set of discrete points within our illumination circle, each appropriately displaced by some $\vec{r}$ from the illuminating circle center, and I_P is the exiting photon distribution at displacement $\vec{r}$ from the source point P.

D. Tissue Models

The tissue models used these simulations are based on hemoglobin bearing systems which are not necessarily specific to any particular organ but are clinically significant in many highly perfused areas of the body. We will observe the results of a single-layered, semi-infinite slab of oxyhemoglobin (O_2Hb), which absorbs and also is forward scattering. Two scenarios will be discussed: an optically thick layer, and a thin layer backed by a reflector. The thick layer has a physical thickness of 2 mm, deep enough that most of the light does not penetrate this far. The thin layer has a thickness of 250 μm and is backed by a wavelength independent specular reflector which reflects 50% of the light. A reflector based upon the scleral model of Delori is also considered[4].

In this initial study, we set g = 0.99 independent of wavelength, which reflects the extremely forward-scattering nature of blood[10]. This is most easily seen by adopting the notion of mean trajectory from the photon diffusion literature. The choice of g directly affects the mean trajectory of photons within the tissue (and therefore the distribution of free space trajectories after exiting the surface). As g approaches unity, the curvature of the mean trajectory decreases.

The simulations performed in this study use $4 \cdot 10^4$ photon packets per wavelength, covering the spectral range between 451-1000 nm at a resolution of 3 nm. This is a tremendous computational burden that we would hope to minimize by further code optimization.

3. Results & Discussion

The simple case of the optically thick layer of oxyhemoglobin, illuminated by a monochromatic pencil of photon packets, shows the effect of photon migration at wavelengths with low attenuation. We show the backscatter as a function of wavelength in Figure 1, simulating the output of an image detector placed directly on the surface of the tissue. In the blue and green parts of the spectrum, the apparent diameter of the backscattering region is small compared to that found in the red. One clearly sees the effect of illuminating a small surface region upon the neighboring areas which passively re-radiate diffused light. For clarity, the optical properties of oxyhemoglobin are also shown in Figure 1.

A. Effects of Wavelength on Path Length Distributions

We first investigate photon trajectories by assuming pencil illumination of photon packets normally incident upon the tissue surface. A detector positioned at different displacements from the packet entry point collects backscattered packets and their histories. Tracking the course of the photons through the tissue reveals the approximate volume of tissue sampled by our experiment, as well as an indication of the relative

number of photons scattered into adjacent pixels. Knowing the probability distributions of the photons will also eventually aid in spectral analysis in more complex targets, such as multilayered systems[11]. The results at four source-detector separations for a thick oxyhemoglobin layer are shown in Figure 2. In addition to the results simulated at g=0.99, a second set of plots from a simulation at g=0.95 are presented for comparison purposes. The photon distribution functions are largely the same, and we restrict futher discussion to the more forward-scattering case. As noted by Cui et al., the distributions show that the low absorption wavelengths that penetrate deeper have a much larger variation in their path lengths and should account for more contamination into adjacent image pixels[12].

B. Effect of illumination size

Since the longer wavelengths experience less attenuation in hemoglobin, wider illumination spots sizes increase the apparent backscatter at longer wavelengths, as shown in Figure 3. This figure presents the light exiting the center of an illuminated circle of successively larger diameters. For clarity, the plots are all normalized to the same value at an arbitrary wavelength in a highly absorbing part of the spectrum. The spectral distortion illustrated beyond 590 nm is the inverse of the spatial spreading effect depicted in Figure 1. In Figure 4, the change in backscatter is plotted as a function of illumination disk diameter at wavelengths of low and high absorption.

The previous figures depict results from an image detector in contact with the tissue surface. While this is an illustrative *gedanken* experiment, it is more realistic to discuss an imaging optic and detector plane spaced away from the tissue surface. In this case, the

angular field of view becomes an issue and only a fraction of backscattered photons actually participate in image formation. We observe the effect of extended photon trajectories numerically by excluding from the above result (at 0.6 mm illumination beam diameter) those photons that have traveled more than a given distance. By limiting the maximum allowed path lengths to several values, we reduce the effects of illumination from surrounding pixels so that the spectrum associated with a pixel results from a smaller surrounding volume. The effect is similar to that achieved by collapsing the measurement from the imaging case to a single point reflectivity measurement. As we approach the shorter allowable path lengths shown in Figure 5, we see that the shape of the wavelength intensity profile resembles the first order Beer's law approximation, which has the shortest allowed path length.

C. Effect of imaging at finite angular fields of view

When using a limiting aperture for light collection, the spectrum of backscattered light changes its shape. Figure 6 summarizes the spectral effects of the entrance pupil diameter. Not only does the effect at the less attenuated wavelengths become more pronounced, but the amount of light captured by smaller fields of view reduces the numerical signal-to-noise ratio. The additive affect of the longer wavelengths can be viewed as a consequence of the "banana"-shaped mean photon trajectories[13]. On average, in forward scattering tissue such as O_2Hb, packet trajectories that penetrate further bend back more to the normal direction by the time they exit the tissue surface. The closer to the surface normal the distribution of the exiting angles, the higher the probability of collection through the entrance pupil.

The distribution of exit angles from the surface at each wavelength shown in Figure 7 illustrates this point. This data is taken from the same simulation run used to produce Figure 6. The distribution of exiting angles from the single slab case peaks around 45 degrees, causing many of the photons to miss the entrance pupil. The less attenuated wavelengths show a tendency to exit closer to the normal, as well as a higher number of exiting photons.

D. Comparing Tissue Models

So far we have treated the simple case of photons allowed to wander through an optically thick medium. To further investigate the effects of photon trajectories, we place a specular reflector behind a thin layer of oxyhemoglobin. This could, for example, represent a simplified model of the scleral layer backing the choroid of the retina. In comparison with the thick layer, we consider both a scleral model from the literature as well as a wavelength independent reflector model. The thickness for the thin layers is held at 250 μm, which is close to the thickness of the choroidal layer behind the retina. Both of the back reflectors are modeled as pure specular reflectors. The neutral model's reflectivity is 50% at all wavelengths, while the reflectance of the scleral model has an empirically derived wavelength dependence taken from the work of Delori[4] to be

$$R_{sclera}(\lambda) = 0.5 \cdot \exp(-.00261 * (\lambda - 675)).$$

In the context of comparing these models, we will only look at the wavelength range between 450-750 nm. Figure 8 shows the results of all three tissue models, where light over 2π steradians is collected.

It is instructive to consider the ratio of backscattering from a reflector-backed model to the backscatter from the optically thick model. Figure 9 displays the results of dividing the measured spectra of the neutral reflector by that of the optically thick layer at two angular fields of view. Figure 10 shows the results of dividing the measured spectra from the 23.58° collection angle by the 90° collection angle (tissue surface mounted detector array). This ratio represents the relative magnitude of bias for certain wavelengths in each model considered.

4. Conclusions

By definition, spectral imaging requires illumination of the entire region of interest. For any pixel within this region, optical scattering generates photon fluxes in and out of the region's underlying volume element. The magnitude of this effect varies with scattering cross section and mean free path. Where absorption is low, the notion of point-by-point spectroscopy must be replaced by the concept of regional spectral contamination. Since the optical properties of a tissue govern the length and shape of the photon paths, the imaging system itself will play an important role. The effect of a entrance pupil is twofold. First, the longer path length photons have more ability to bend back toward the normal because they experience more scattering events, but lower overall attenuation. Since the angular distribution is centered roughly around 45°, these wavelengths appear to be more highly backscattered when light collection is limited to narrower angular fields of view. When image features become significant, the additional spectral content in one pixel will become still more complex than in the homogenous, single-slab tissue case presented here.

5. Acknowledgements

We gratefully acknowledge Cedars-Sinai Medical Center for funding this research, the Jet Propulsion Laboratory for access to their Cray90 computing resources, and to Steven Jacques for his correspondence and for making Monte Carlo code publicly available.

Figure Captions

Figure 1:

Wavelength-resolved backscatter imaging demonstrates the relative effects of photon migration that occurs in a single oxyhemoglobin layer. In these images, the magnitude of the backscatter is represented on a grayscale with black being the most intense, white equaling zero signal. These images correspond to the data from a ccd chip placed directly on the tissue surface where illumination is from an infinitely narrow collimated source located at (0,0). The line plot shows the wavelength-resolved absorption and scattering coefficients of oxyhemoglobin used throughout this paper, in units of cm^{-1}.

Figure 2:

Distributions of exiting photon packets from an optically thick single layer of oxyhemoglobin (2 mm) as a function of path length at radial distances away from the pencil illumination source. The solid lines represent a high absorptive wavelength (562 nm); the dotted lines represent a low absorptive wavelength (λ=649 nm).

Figure 3:

Effect of illumination size on backscatter data from a single-layer of O_2Hb (2 mm thick) viewed from detector positioned at center of beam on the surface. Lines show the results from beam diameters of (a) single point, (b) 0.3 mm, (c) 0.6 mm, (d) 0.9 mm, (e) 1.2 mm, and (f) 1.5 mm from bottom to top, respectively. For comparison purposes the plots are normalized at λ=562 nm.

Figure 4:

Backscatter from the center of illuminated disks of several diameters, at three representative wavelengths. The lines connecting the points serve only as a guide to the eye. At these beam sizes, the increase in backscattered signal at the low absorption wavelength increases linearly with spot diameter.

Figure 5:

Backscatter collected when pathlengths exceeding various threshold values are numerically rejected in the case of a constant beam diameter of 0.6 mm.

Figure 6:

Effect of limiting angular field of view on backscatter data from a single thick layer of O_2Hb (2 mm thick), illuminated by 0.9 mm beam and imaged 10 cm away from surface. All results have been normalized at λ=562 nm.

Figure 7:

Angular distribution of backscattered photons at the surface for high absorption (451 nm on left) and low absorption (751 nm on right). The angle of exit is measured from the normal direction at the surface, not factoring the x and y directional vectors. Illumination extends to 0.45 mm in the radial direction.

Figure 8:

Comparing backscatter of O_2Hb models as viewed from a surface detector positioned at center using a 0.9 mm illumination beam. Plots show results from a scleral reflector, a neutral 50% reflector, and a thick layer (2 mm), which have been normalized at λ=562 nm.

Figure 9:

Ratio of backscatter from thin oxyhemoglobin layer backed by a neutral reflector to backscatter from optically thick layer of oxyhemoglobin. Backscatter measured at center of illumination disk using a 0.9 mm diameter beam. Shown for two angular fields of view.

Figure 10:

Comparison of ratio models (scleral reflector, 50% reflector, and thick layer) at $r = 0$. Plots show ratio of result at 23.6° acceptance half-angle to 90° acceptance half-angle.

REFERENCES

[1] see for example the recent review G. A. Wagnieres, W. M. Starr, B. C. Wilson, "*In Vivo* Fluorescence Spectroscopy And Imaging For Oncological Applications", *Photochem. and Photobiol.* **68**(5), pp. 603-632 (1998).

[2] R. M. Levenson and D. L. Farkas, "Digital Imaging Spectroscopy For Histopathology And Cytopathology", Proc. SPIE **2893**, pp. 13-135 (1997).

[3] R.O.Green, M.L.Eastwood, C.M. Sarture, T.G. Chrien, M.Aronsson, B.J. Chippendale, J.A. Faust, B.E. Pavri, C.J. Chovit, M. Solie, M. R. Olah, and O.Williams, "Imaging Spectroscopy And The Airborne Visible/Infrared Imaging Spectrometer", *Remote Sens. Environ.* **65**, pp. 227-248 (1998).

[4] F.C. Delori and K.P. Pfilbsen, "Spectral Reflectance of the Human Ocular Fundus," *Appl. Opt.* **28**(6), pp. 1061-1076 (1989).

[5] M. Hammer, D. Schweitzer, L. Leistriz, M. Scibor, K-H Donnerhacke, J. Strobel, "Imaging Spectroscopy of the Human Ocular Fundus *In Vivo*", *J. Biomed. Opt.* **2**(4), pp. 418-425 (1997).

[6] W. Grundfest, D. Cohen, T. Papaioannou, G. Bearman, and R. Novack, "Imaging Spectroscopy of the Retina," Annual Meeting, Optical Society of America, Long Beach (1997).

[7] L.-H. Wang, S.L. Jacques, and L.-Q. Zheng, "MCML – Monte Carlo modeling of Photon Transport in Multi-Layered Tissues," *Computer Methods and Programs in Biomedicine* **47**, pp. 131-146, (1995).

[8] B. J. Tromberg, L. O. Svaasand, T-T. Tsay, R. C. Haskell, "Properties of Photon Density Waves in Multiply-Scattering Media", *Appl. Opt.*, **32**(4) pp. 607-616 (1993).

[9] D.T. Delpy, M. Cope, P. van der Zee, S. Arridge, S. Wray, and J. Wyatt, "Estimation Of Optical Pathlength Through Tissue From Direct Time Of Flight Measurement," *Physics in Medicine and Biology*, **33**(12), pp. 1433-1442 (1988).

[10] A. Roggan, M. Friebel, K. Dorschel, A. Hahn, and G. Muller, "Optical Properties Of Circulating Human Blood," Proc. SPIE v. 3252, pp. 70-82 (1998).

[11] R.F Bonner, R. Nossal, S. Havlin, and G.H. Weiss, "Model For Photon Migration In Turbid Biologic Media," *JOSA A*, **4**(3), pp. 423-432 (1987).

[12] W. Cui, N. Wang, and B. Chance, "Study Of Photon Migration Depths With Time-Resolved Spectroscopy," *Opt. Let.*, **16**(21), pp.1632-1634 (1991).

[13] S. Feng, F. Zeng, B. Chance, "Monte Carlo Simulations of Photon Migration Path Distributions in Multiple Scattering Media", Proc. SPIE v. **1888**, pp. 78-89 (1993).

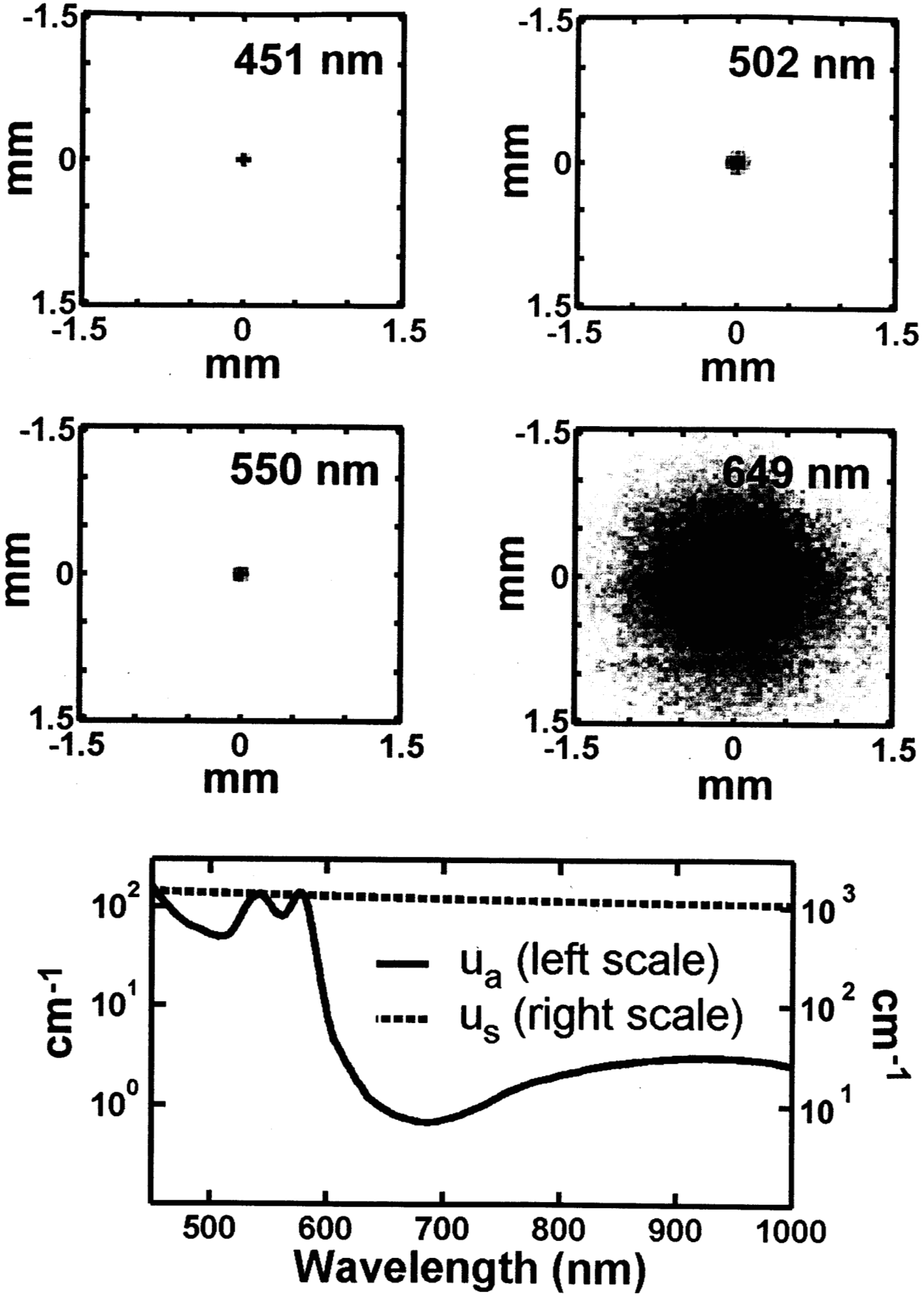
451 nm
502 nm
550 nm
649 nm
-1.5
0
1.5
mm
10^2
10^1
10^0
10^3
cm-1
u_a (left scale)
u_s (right scale)
500
600
700
800
900
1000
Wavelength (nm)

Figure 1 not

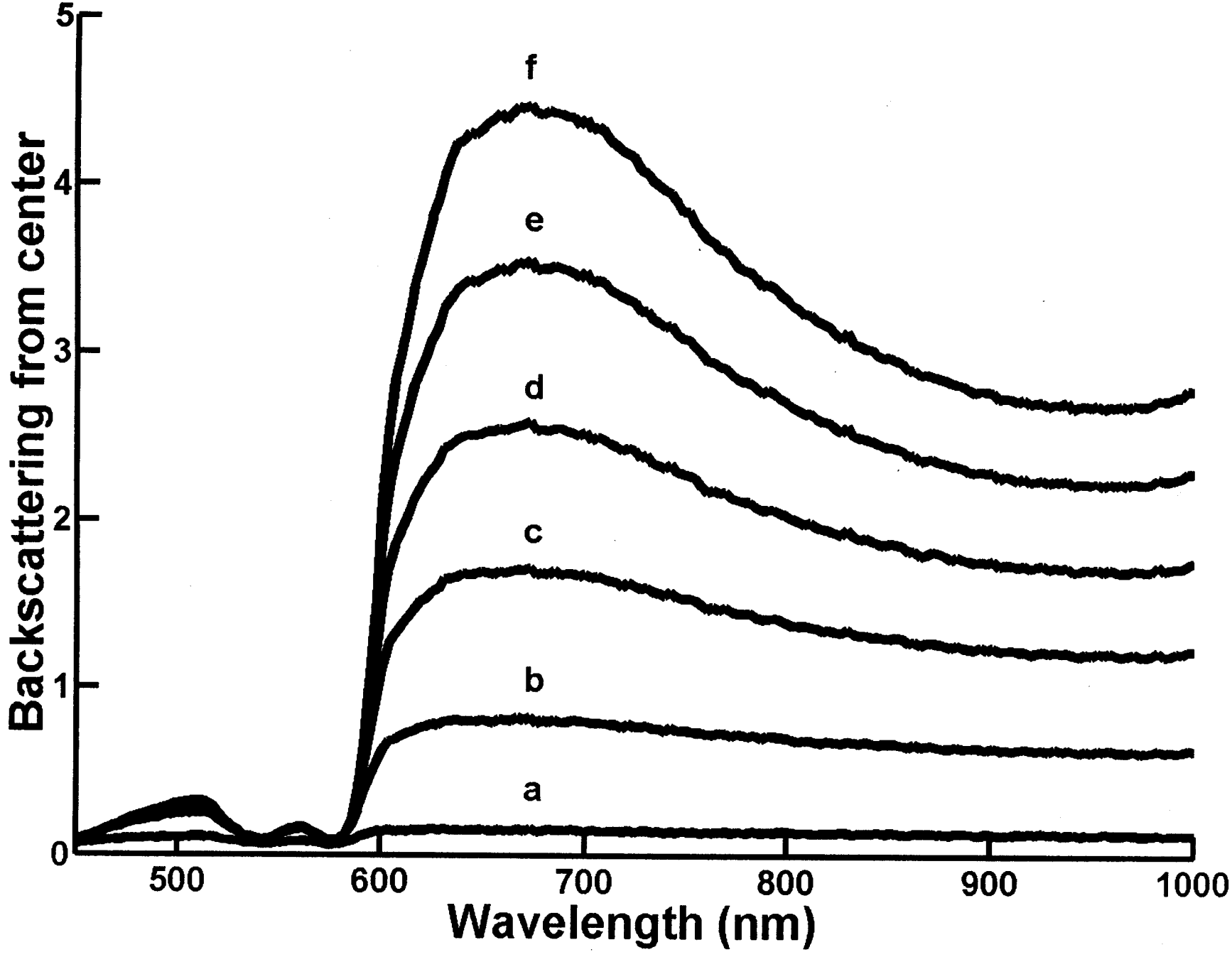
Backscattering from center
Wavelength (nm)
0
1
2
3
4
5
500
600
700
800
900
1000
a
b
c
d
e
f

Figure 3 up↑

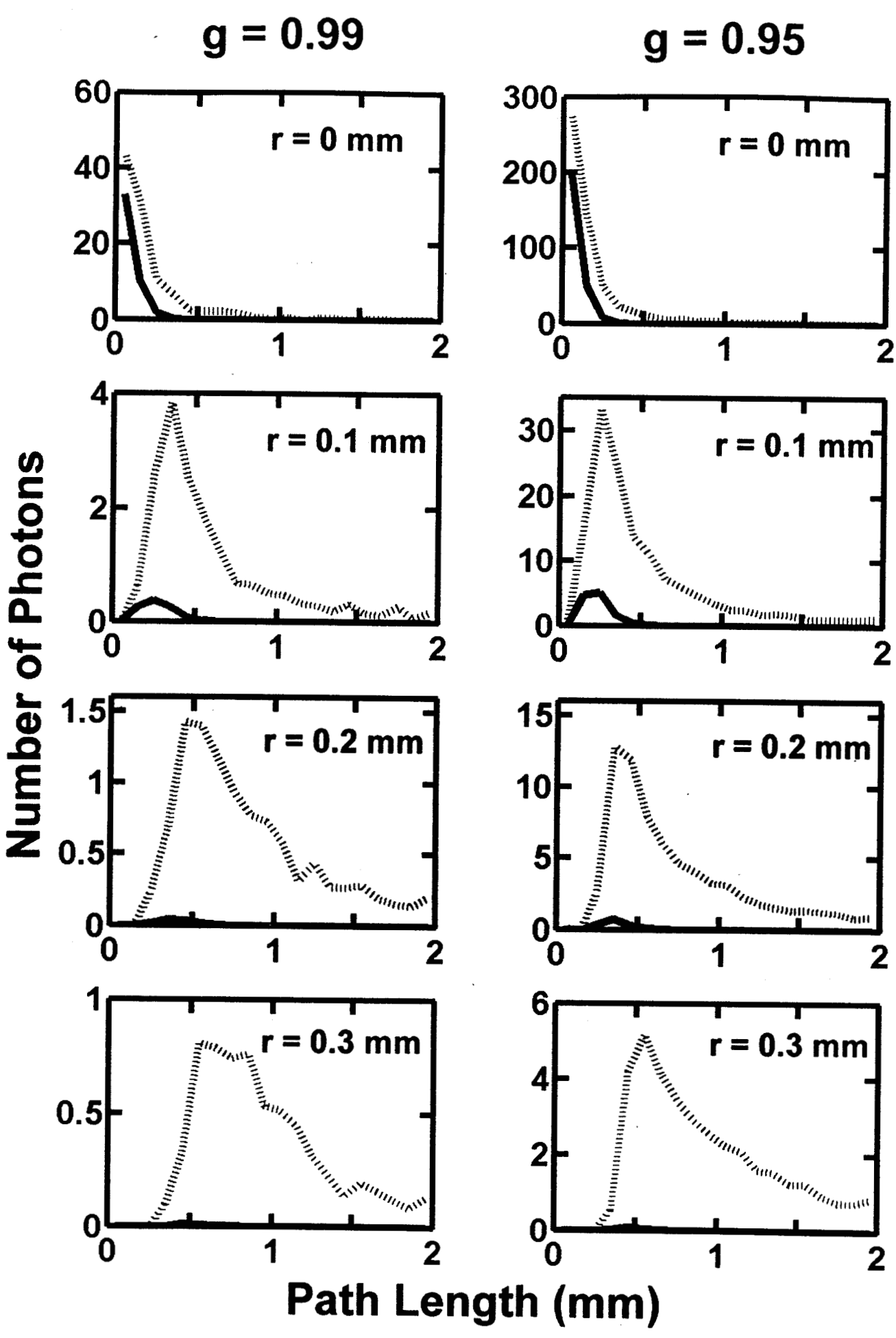
g = 0.99
g = 0.95
r = 0 mm
r = 0.1 mm
r = 0.2 mm
r = 0.3 mm
Number of Photons
Path Length (mm)

Figure 2 not

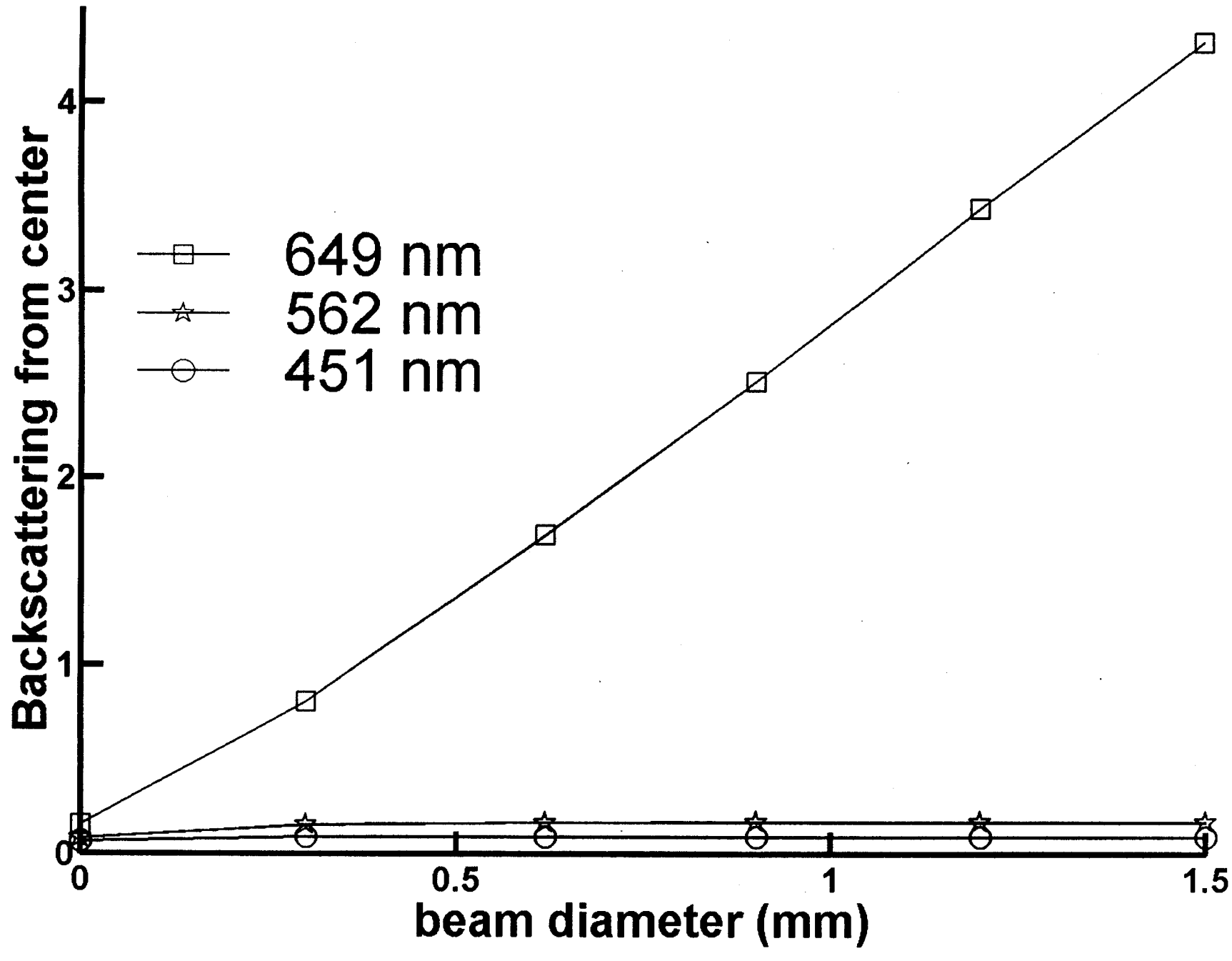
Backscattering from center
4
3
2
1
0
649 nm
562 nm
451 nm
0
0.5
1
1.5
beam diameter (mm)

Figure 4 not↑

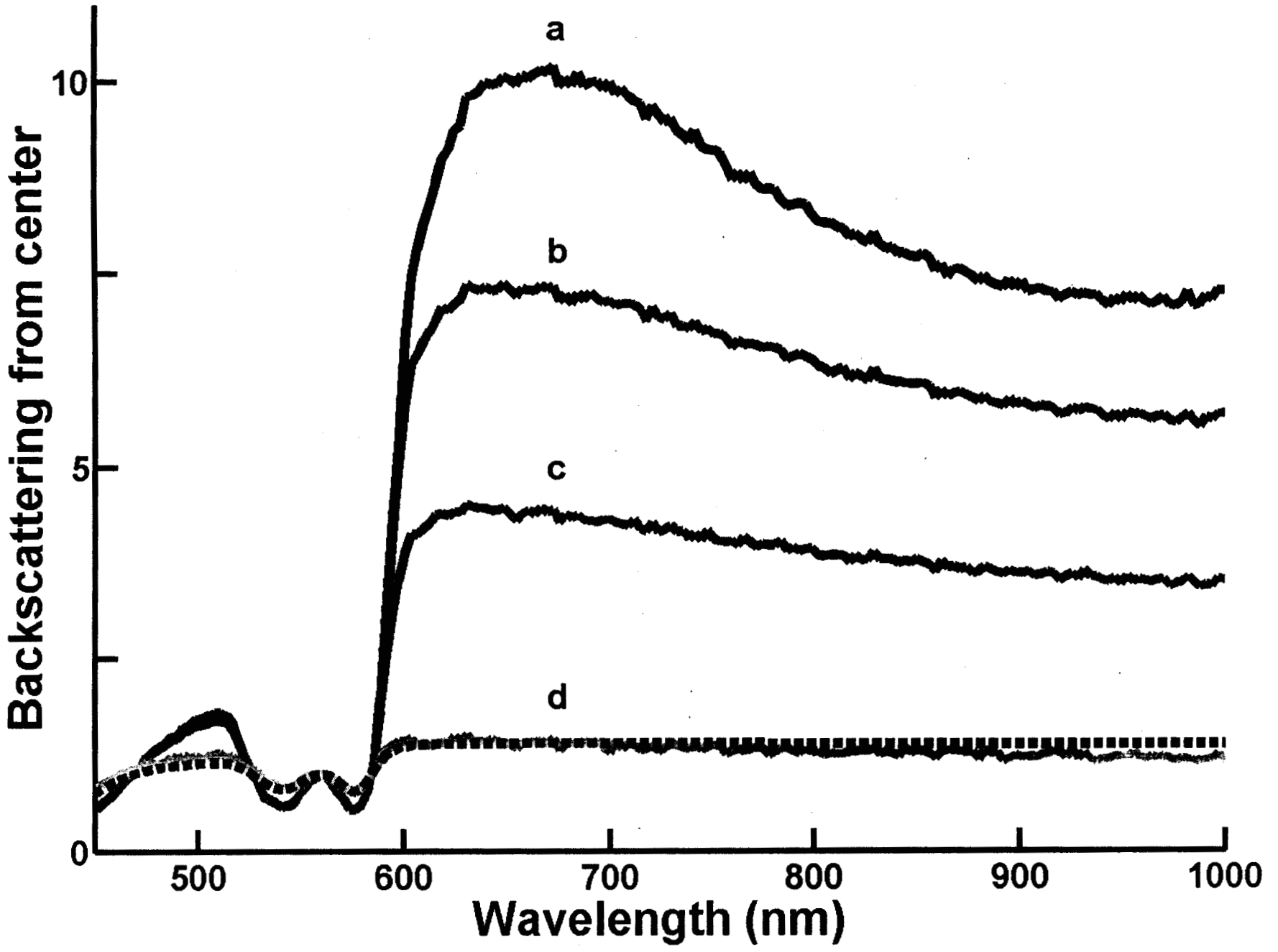
a
b
c
d
10
5
0
Backscattering from center
500
600
700
800
900
1000
Wavelength (nm)

Figure 5 and

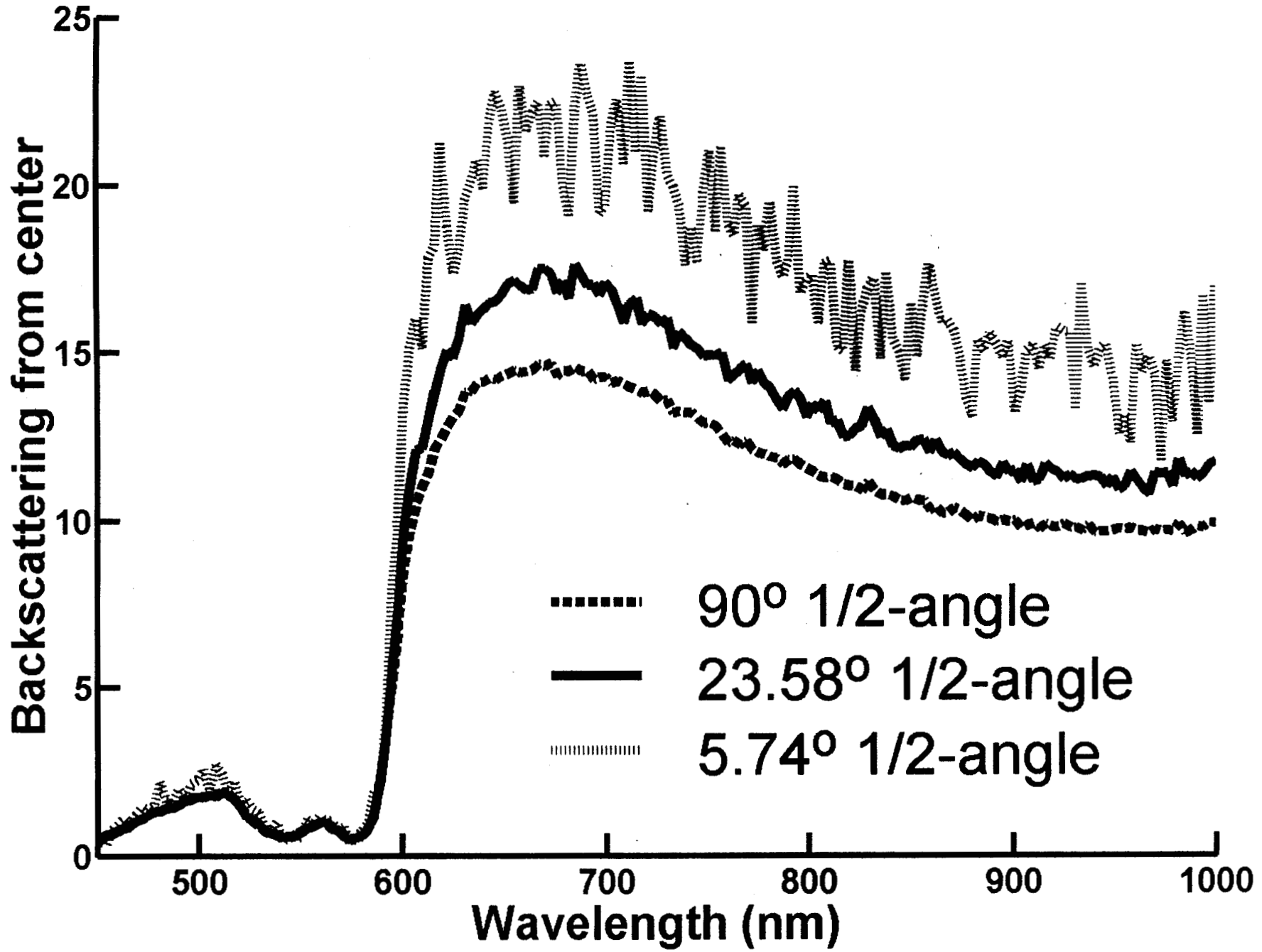
Backscattering from center
25
20
15
10
5
0
500
600
700
800
900
1000
Wavelength (nm)
90° 1/2-angle
23.58° 1/2-angle
5.74° 1/2-angle

Figure 6 up↑

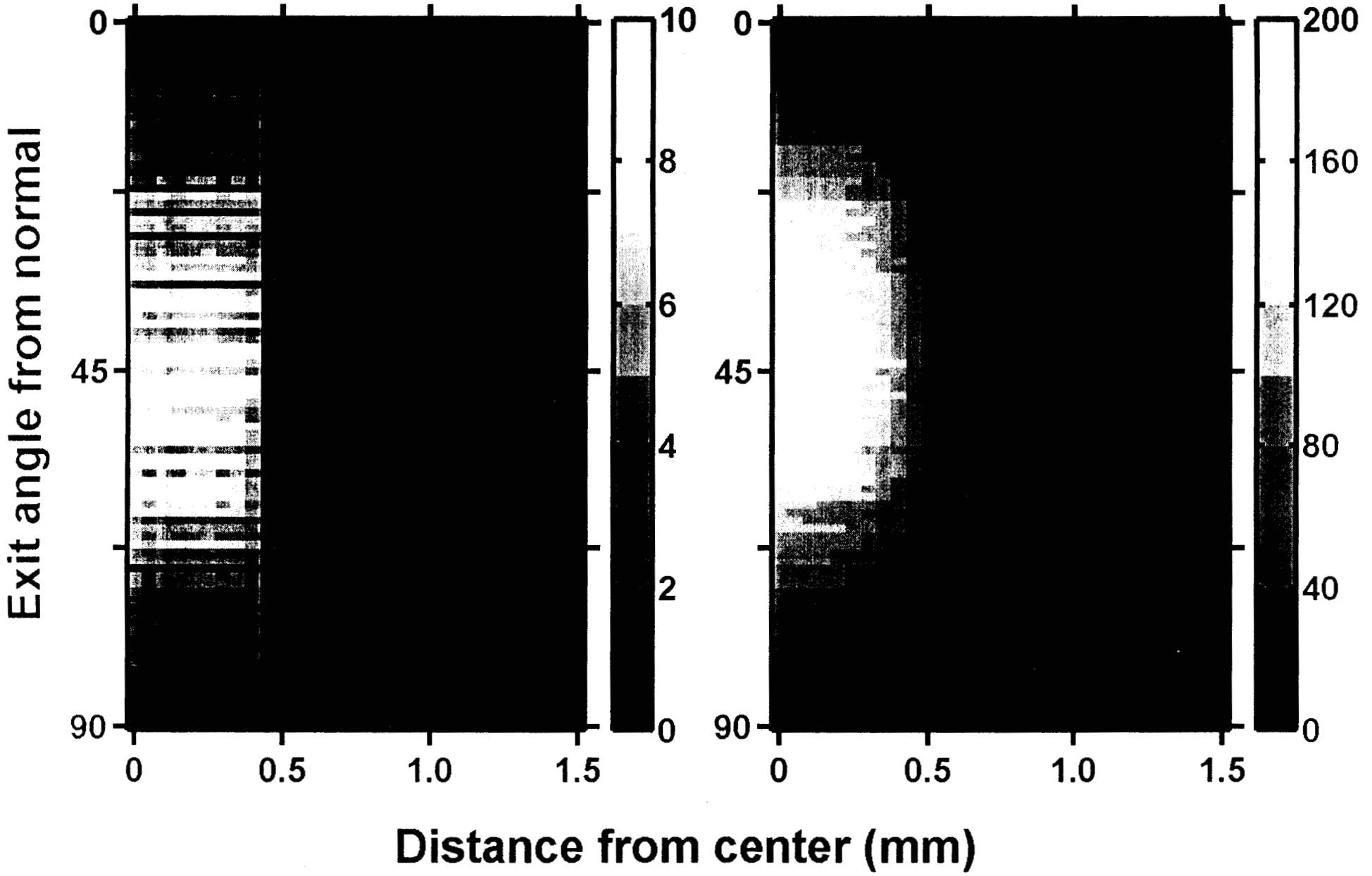
Exit angle from normal
0
45
90
0
0.5
1.0
1.5
Distance from center (mm)
10
8
6
4
2
0
200
160
120
80
40
0

Figure 7 UP↑

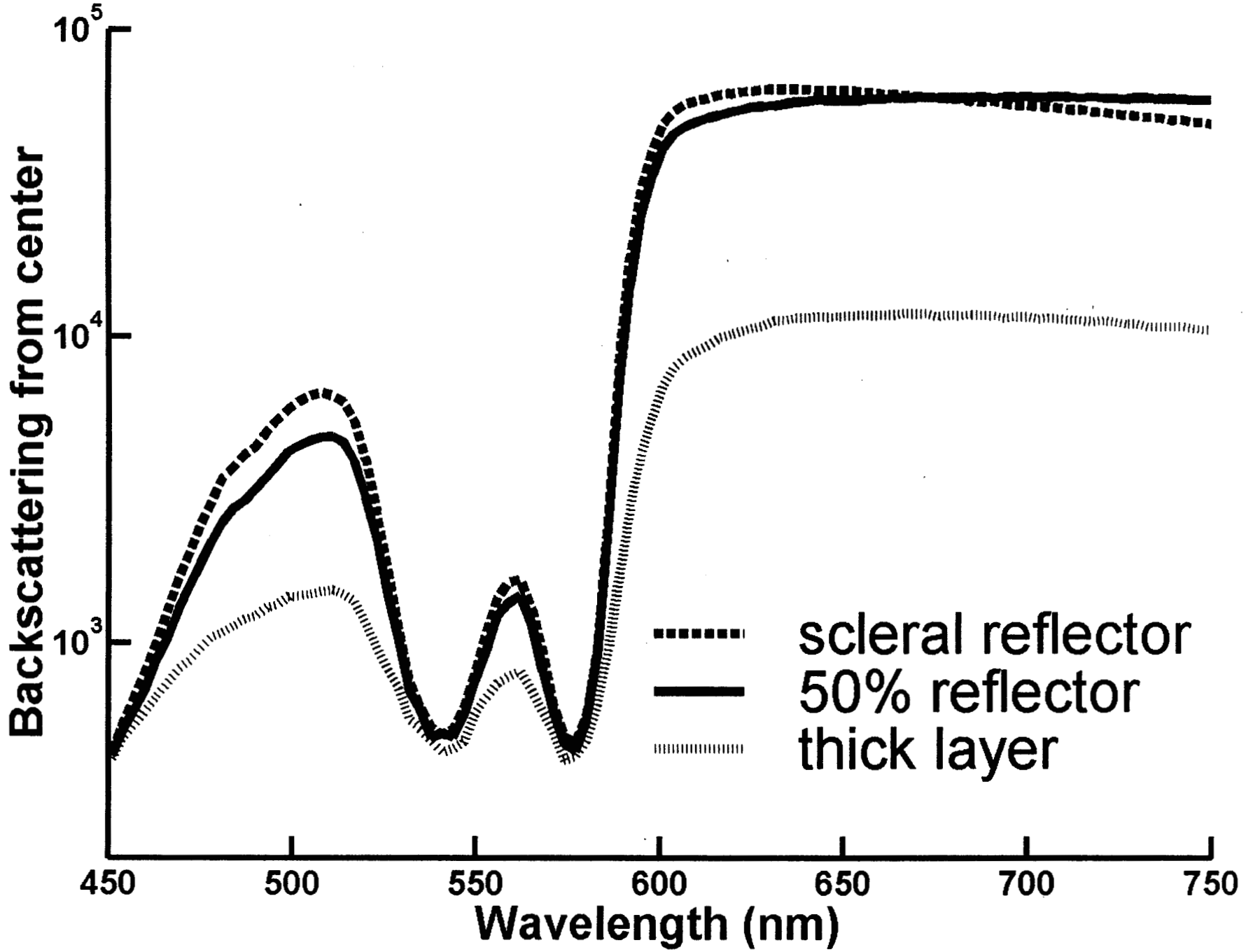
Backscattering from center
10^5
10^4
10^3
450
500
550
600
650
700
750
Wavelength (nm)
scleral reflector
50% reflector
thick layer

Figure 8 up ↑

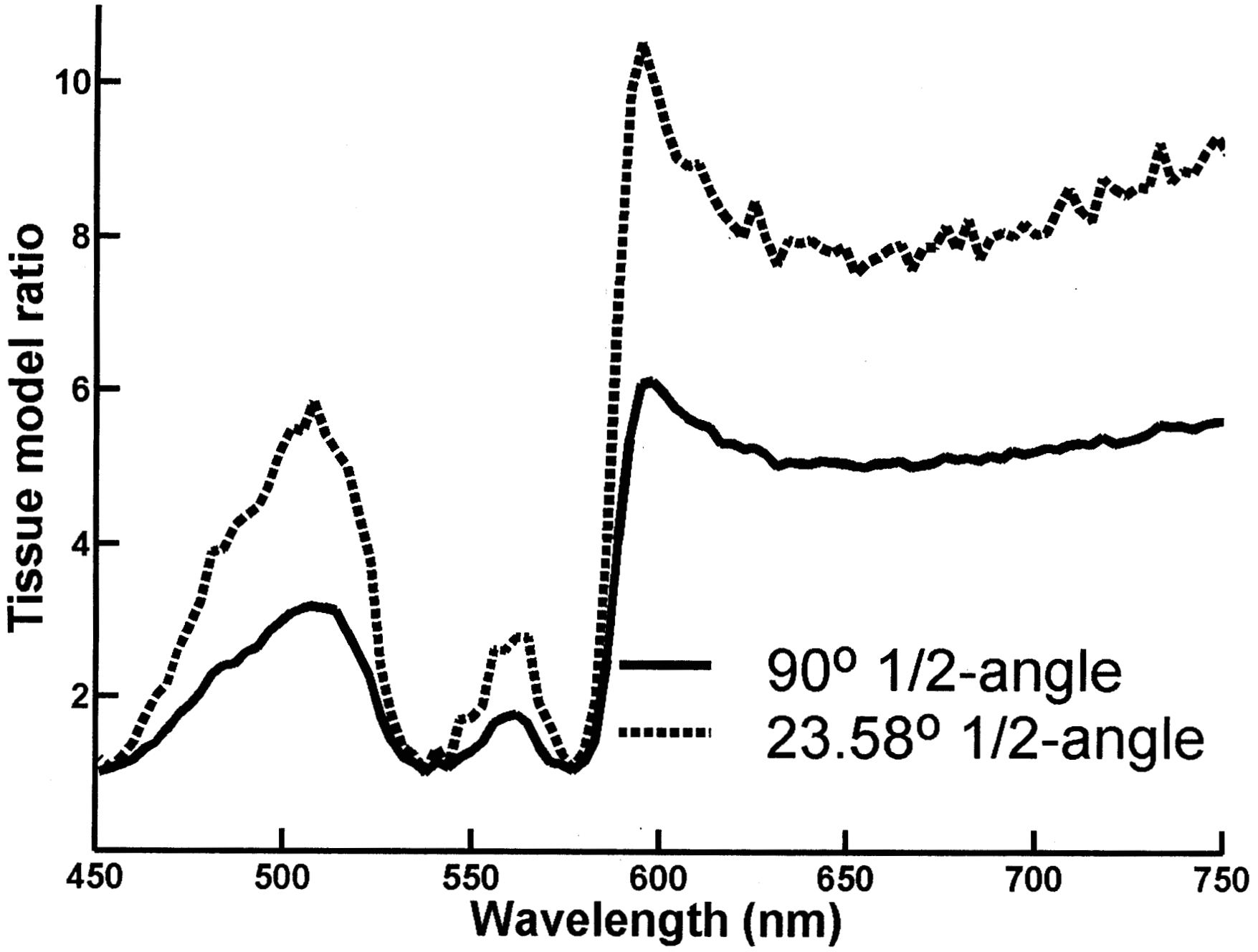
Tissue model ratio
10
8
6
4
2
450
500
550
600
650
700
750
Wavelength (nm)
90° 1/2-angle
23.58° 1/2-angle

Figure 9 ↑

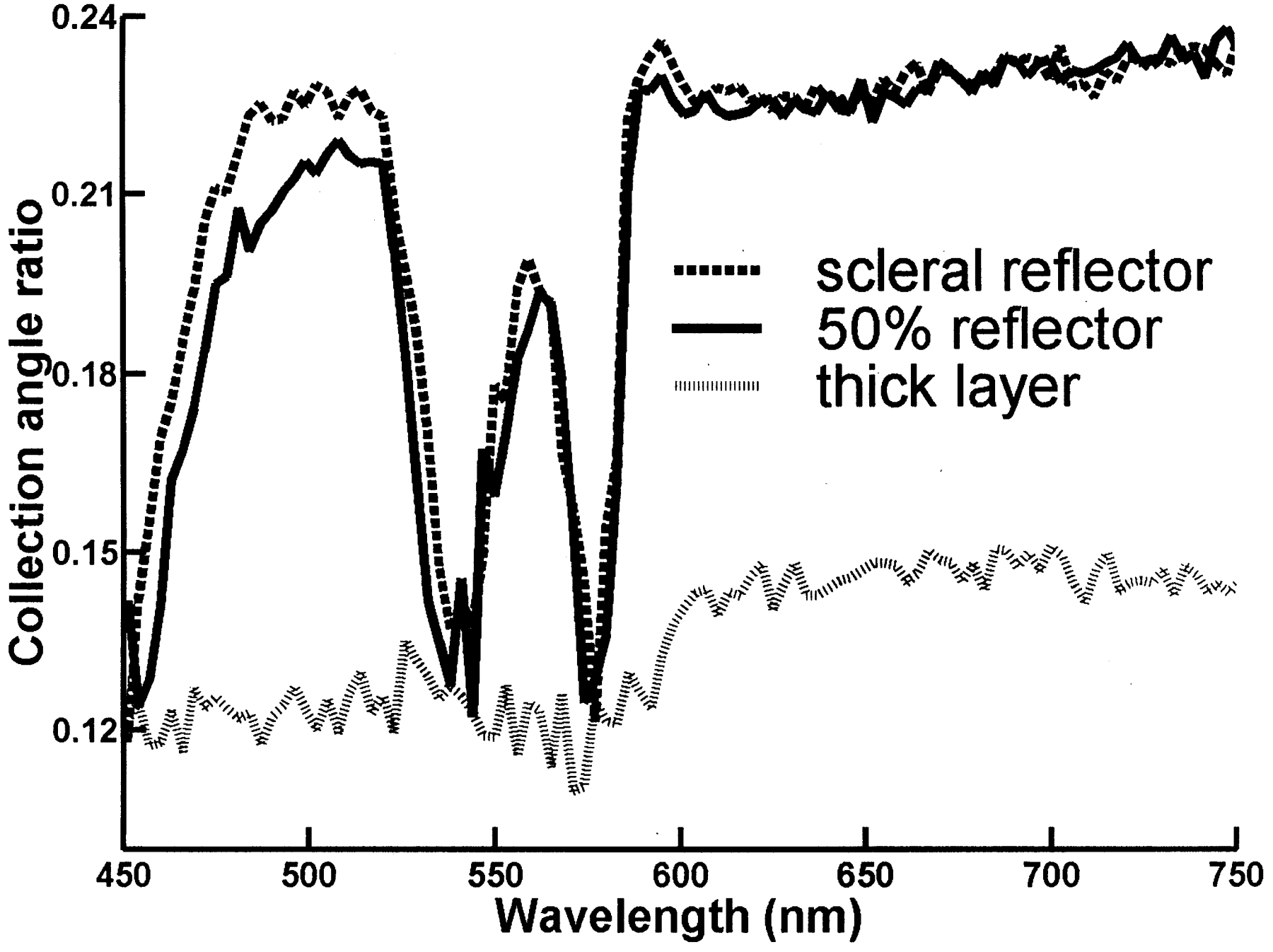
0.24
0.21
0.18
0.15
0.12
Collection angle ratio
scleral reflector
50% reflector
thick layer
450
500
550
600
650
700
750
Wavelength (nm)

Figure 10 up↑